ChemElectroChem

Research Article
doi.org/10.1002/celc.202300460

Chemistry Europe
European Chemical Societies Publishing

www.chemelectrochem.org

Nickel and Commercially Available Nickel-Containing Alloys as Electrodes for the Electrochemical Oxygen Evolution

Nikolas Mao Kubo,[a] Fabian Ketter,[a] Stefan Palkovits,[a] and Regina Palkovits*[a, b]

This work is dedicated to Prof. Marcel Liauw on the occasion of his 60th birthday.

Water electrolysis is a crucial technology for independency on fossil fuels. However, water splitting is limited by the sluggish kinetics of oxygen evolution reaction (OER). While many studies report highly active, non-precious metal-based electrocatalysts for alkaline OER, applicability under industrial conditions is often omitted. Such conditions require catalysts being applied on nickel or nickel-containing alloys in elevated electrolyte concentrations. In contrast to the rather inert substrates often used in scientific studies, such industrially applied substrates exhibit significant OER activity themselves and show dynamic behaviour. Therefore, it is crucial to understand the OER behaviour of such substrates. Here, nickel and seven commercially available nickel-containing alloys are investigated as anodes in alkaline OER and their elemental compositions correlated to their corresponding activities. Repeated potential cycling across the Ni(II)/Ni(III)-redox couple is established as activity-enhancing procedure. Overall, the nickel-base alloy Hastelloy® X exhibits the highest activity due to its Fe-, Cr-, Mo- and Co-content. Though, the activity gain differs significantly for the various materials. Comparing Ni and Hastelloy® X as least and most active materials, the positive impact of activation on both activity and stability becomes evident. While untreated Ni suffers from poor OER stability, the activity-enhancing procedure also significantly increases electrode stability in 24 h chronopotentiometry.

Introduction

In the transition towards a hydrogen-society and -economy independent of limited fossil fuels, electrocatalytic water splitting (i.e., water electrolysis, Equation 1) plays a crucial role as a key technology for the production of hydrogen.[1–4]

$$2\ H_2O \rightarrow 2\ H_2 + O_2 \quad (1)$$

When using power from renewable energy sources for this electrolysis, hydrogen is regarded a sustainable and ecologically friendly energy carrier.[4,5] Therefore, utilizing hydrogen as chemical energy storage can be one solution to solve the shift between energy demand and the intermittent production of renewable energy.[5] Generally, different methods enable the electrolysis of water, with solid electrolytes applied at elevated temperatures in solid oxide electrolysis cells (SOEC) and aqueous electrolytes at lower, near ambient temperatures.[6–9] Here, the proton-exchange membrane (PEM) electrolysis operates in acidic conditions where protons are transferred across a perfluorinated membrane.[6–9] In contrast to PEM, alkaline water electrolysis (AWE) is less reliant on precious metals and proceeds in an aqueous solution of about 30 wt. % KOH as electrolyte.[6–8,10]

A fundamental bottleneck for the overall water splitting technology yet to overcome is the sluggish kinetics of the anodic oxygen evolution reaction (OER), a four-electron-transfer reaction, shown in Equation 2 for alkaline media.[11–13]

$$4\ OH^- \rightarrow O_2 + 2\ H_2O + 4\ e^-$$
$$E^0 = 1.23\ V\ vs.\ RHE \quad (2)$$

For the OER, iridium- and ruthenium-based materials have been identified early as highly active electrocatalysts.[14–16] However, the scarcity of such precious metals limits the large-scale application of water electrolysis.[17] Among non-precious, earth-abundant transition metals, iron-, cobalt- and especially nickel-based compounds have been identified to exhibit low overpotentials and, thus, high activities in OER electrocatalysis.[12,18–22] Many highly active catalysts developed in various research groups are reported in literature. In order to allow for a scientifically precise characterisation, it is good practice to test powdered catalysts ink-casted on highly polished materials like glassy carbon, fluorine-doped tin oxide, titanium or gold, commonly implemented in a rotating disk electrode geometry with well-known mass-transport characteristics.[12,20–23] However, different reports have been

[a] N. M. Kubo, F. Ketter, Dr. S. Palkovits, Prof. R. Palkovits
Institute of Technical and Macromolecular Chemistry
RWTH Aachen University
Worringerweg 2, 52074 Aachen, Germany
E-mail: palkovits@itmc.rwth-aachen.de

[b] Prof. R. Palkovits
Institute for a Sustainable Hydrogen Economy
Forschungszentrum Jülich
Am Brainenergy Park, 52428 Jülich, Germany
E-mail: r.palkovits@fz-juelich.de

Supporting information for this article is available on the WWW under https://doi.org/10.1002/celc.202300460

published, critically questioning these well established and recommended practices due to potentially adverse effects and artifacts influencing the electrochemical characterisation.[24–28]

Whilst scientific understanding of the catalyst properties is highly important, technical and industrial applicability should be considered in a next step to facilitate the large-scale deployment of water electrolysis. Here, one important aspect is the transfer towards catalyst testing on industrially relevant substrates including nickel and nickel-base alloys for application in AWE. As these materials exhibit significant OER activity themselves, it is necessary to be aware of the OER behaviour of these substrates.

While few early works studied the OER behaviour and possible activation methods of metals and metal alloys,[29–31] especially in the last two decades, the groups of Abreu[32,33], Chatenet[34–36], Schäfer[37–39] and Todoroki[40,41] have studied the OER behaviour and performance of commercially available stainless steels as well as different thermo- and electrochemical activation methods. However, as most of these works focus on iron-base alloys, little to no studies can be found on the OER behaviour of nickel-base alloys. Therefore, this work aims to provide a systematic characterisation of the OER behaviour of different commercially available nickel-containing alloys in comparison to nickel. For this purpose, nickel, the nickel-base alloys Alloy 400 (A4), Haynes® 230 (HY), Hastelloy® C22 (HC), Inconel® X750 (IX), Hastelloy® X (HX) as well as the iron-base, nickel-containing alloys AISI 316 Ti (AT) and AISI 303 (A3) are studied here. The activity of the substrates is determined from linear sweep voltammetry (LSV). The content of other present elements and especially of Fe in the alloys is correlated to their activities as the presence of Fe and the other elements in nickel-based OER catalysts is reported to be activity enhancing.[42–52] Furthermore, the metallic substrates show dynamic behaviour themselves and, thus, an activity-enhancing activation procedure is tested. The time-dependent behaviour of the OER activity is recorded for nickel and Hastelloy® X via galvanostatic chronopotentiometry (CP) in standard conditions often applied in scientific reports for the characterisation of alkaline OER catalysts (1 M KOH electrolyte) and their activity is also tested in 30 wt. % KOH as industrially applied AWE electrolyte.[8,10,17,53]

Results and Discussion

Electrochemical Characterisation

All substrates are electrochemically characterised following a standardised measurement protocol as described in the experimental section. Prior to the activity measurements, 30 conditioning cyclic voltammograms (CVs) in the non-Faradaic potential region between 0.4 and 1.2 V vs. the reversible hydrogen electrode (RHE) are recorded. The catalytic activity of the electrode substrates is determined from the forward scans of CVs in the OER overpotential region (> 1.23 V vs. RHE). Each substrate was measured at least twice and Figure 1 illustrates one representative CV for each substrate material. Initially, all

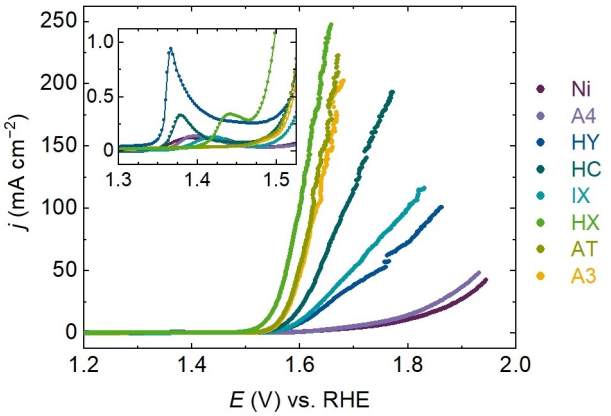

Figure 1. iR-corrected forward scans of cyclic voltammograms (CVs) of all tested substrates show the recorded current densities *j* against the applied potentials *E* measured in 1 M KOH electrolyte at a scan rate of 10 mV s^{-1} in a potential window of 1.2 to 2.0 V vs. RHE. Inset with magnification in the area of 1.3 to 1.5 V vs. RHE and 0 to 1 mA cm^{-2} showing oxidation peaks.

CVs possess very low currents indicating the absence of electrochemical reactions. This absence at applied potentials larger than 1.23 V vs. RHE correlate to activation barriers in the OER requiring larger overpotentials. Above 1.5 V vs. RHE, currents increase at different rates for the different materials. In general, a higher activity correlates to higher recorded current densities *j* and, thus, higher reaction rate at a given applied potential.

Nickel and A4 in comparison to the other substrates exhibit a high onset potential of about 1.6 V vs. RHE and generally low current densities *j* below about 50 mA cm^{-2} (Figure 1). HY and IX reach higher currents of up to about 120 mA cm^{-2} and HC about 200 mA cm^{-2}. A3 and AT show very similar CV behaviour and reach higher current than HC. The highest currents of up to 250 mA cm^{-2}, lowest onset potential of about 1.5 V vs. RHE and, thus, highest activity is found for HX. Any scattering of the CV curves can be attributed to uneven oxygen bubble detachment behaviour. The inset in Figure 1 shows the oxidation peaks observable between 1.3 and 1.5 V vs. RHE. As all materials contain nickel, these peaks can be assigned to the oxidation of Ni(II)- to Ni(III)-species.[53] With different alloying elements, the peak position of this oxidation is significantly shifted,[36,44] which illustrates the influence of the alloying elements on the overall electrochemical behaviour of the nickel-base electrodes and, thus, their OER performance.

One benchmarking parameter for numerical evaluation of the activity is the overpotential η which is defined as the difference between the potential needed to reach a certain current and the equilibrium potential. Thus, a lower overpotential denotes a higher OER activity. In this work, the activity is compared with the overpotential η_{10} determined at the potential applied to reach a current density of 10 mA cm^{-2}. Figure 2b summarizes the overpotentials for all tested substrates. Pure nickel itself exhibits the highest overpotential. This emphasizes that the presence of any second metal among the tested substrates results in an enhanced activity. Figure 2a provides the elemental composition of the tested substrates.

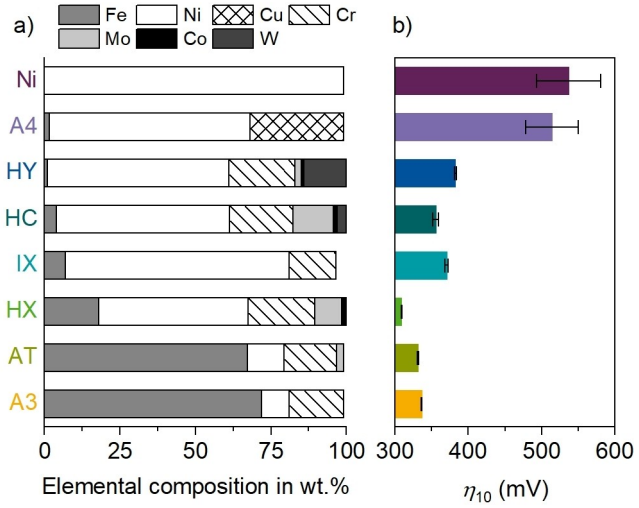

Figure 2. a) Elemental composition of all tested substrates. The total sum of all elements can differ from 100 % as only elements with at least 1 % weight fraction and mean values for compositional ranges are shown. b) Overpotential η_{10} determined from the potential applied to reach a current density of 10 mA cm^{-2} at a scan rate of 10 mV s^{-1} during the forward scan, averaged over at least two measurements. Prior to the activity measurements, 30 conditioning CVs were recorded at a scan rate of 100 mV s^{-1} in the non-Faradaic potential range of 0.4 to 1.2 V vs. RHE.

Here, only the elements with a weight fraction of at least 1 % and mean values of compositional ranges are visualised. A complete table of the elemental composition of the tested substrates is listed in Table S1 in the supplementary information (SI).

The high copper content in A4 does not appear to significantly improve the activity as its overpotential with 514 ± 36 mV is only slightly lower than that of nickel with 537 ± 44 mV. In contrast, the higher contents of 22 wt. % Cr and 14 wt. % W in HY account for a significant decrease of the overpotential to 383 ± 2 mV. Furthermore, the presence of about 1 wt. % Co is expected to facilitate the activity as it is reported as a highly active element for OER electrocatalysis, also in presence of Ni and Fe.[43,54] Fe itself is well reported to exhibit a strong activity enhancing effect on Ni.[44–46] For A4 and HY however, their low Fe contents of 1–2 wt. % do not appear to hold a significant influence on the activity as shown by their highly different overpotentials. IX possesses a lower activity with an overpotential of 371 ± 3 mV, despite its higher Fe content of 7 wt. % compared to HC with 4 wt. % which reaches 356 ± 2 mV. Here, the comparatively high Mo content of about 13.5 wt. % is expected to contribute to the higher activity of HC,[48] possibly further facilitated by the presence of a small Co content of around 1 wt. %. Both, Mo (9 wt. %) and Co (1.5 wt. %) can be found in HX as the most active substrate among all tested materials with an overpotential of 309 ± 1 mV. Moreover, the high Fe content of 18 wt. % enables its superior activity.

Generally, a rough trend of increasing activity with increasing Fe content up to about 18 wt. % for HX can be observed. For iron-base alloys and, thus, much higher Fe contents, the Ni content on the other hand now appears to be too low, as AT and A3 exhibit higher overpotentials of 332 ± 1 and 336 ± 1 mV respectively. However, these comparatively high activities of AT and A3, only second to HX among all tested substrates, underline the activity-promoting effect of the presence of both Fe and Ni, respectively. Further electrochemical characterisation of the materials, including the Nyquist plots of the electrochemical impedance spectra (EIS), are depicted in Figure S2 in the SI.

Influence of elevated KOH concentration. In industrial AWE application, the commonly applied electrolyte concentration of about 30 wt. % (6.9 M) KOH significantly exceeds the KOH concentrations often reported and recommended in scientific OER electrocatalyst characterisation of 1.0 M or even as low as 0.1 M.[10,12,21,22] The usage of elevated KOH concentrations in industrial application can be explained by the conductivity of the electrolyte. At about 30 wt. %, the conductivity of an aqueous KOH solution reaches its maximum.[10] Therefore, direct testing of OER electrocatalysts in elevated electrolyte concentration could facilitate the estimation of industrial applicability. In this work, Ni and HX are tested in 30 wt. % KOH. Equal to the testing protocol in 1 M KOH, the electrodes are initially conditioned by 30 CVs in a non-Faradaic potential region between 0.4 and 1.2 V vs. RHE at a scan rate of 100 mV s^{-1}. Consecutively, CVs are recorded at a scan rate of 10 mV s^{-1} between 1.2 and 2.0 V vs. RHE for activity assessment. The forward scans of these CVs are depicted in Figure 3.

Generally, higher currents are reached in elevated KOH concentrations. It can be assumed that the higher concentration of hydroxyl anions facilitates mass transport, resulting in higher currents. Furthermore, the onset potentials of the OER remain roughly at the same position. This indicates that the increased KOH concentration does not significantly influence the activation barrier of the OER. This is especially the case for HX, as both CVs show similar shapes with the one in 30 wt. % KOH reaching almost twice the current density (at 1.65 V vs. RHE 232 mA cm^{-2} in 1 M KOH compared to 428 mA cm^{-2} in 30 wt. % KOH). For Ni however, the CV recorded in 30 wt. % KOH possesses a different shape. Despite a similar onset potential

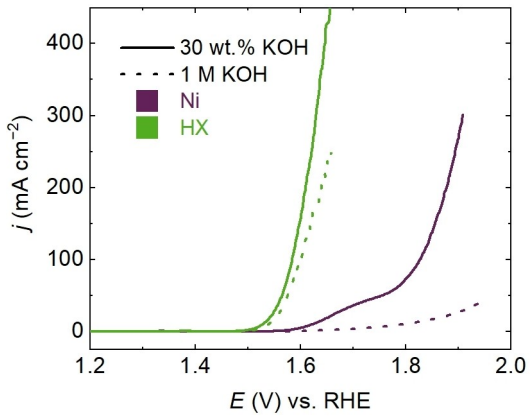

Figure 3. iR-corrected forward scans of cyclic voltammograms (CVs) of Ni and Hastelloy® X measured in 30 wt. % KOH electrolyte (solid line) and in 1 M KOH (dotted line) at a scan rate of 10 mV s^{-1} in a potential window of 1.2 to 2.0 V vs. RHE.

around 1.6 V vs. RHE, an anodic shoulder is visible at about 1.7 V vs. RHE after which the current strongly increases. While in 1.0 M KOH a current density of 27 mA cm^{-2} is reached at 1.90 V vs. RHE, 272 mA cm^{-2} is reached in 30 wt. % KOH, corresponding to a ten-fold increase. This different CV shape as well as the significant gain in current could potentially indicate different mass transport characteristics or a different OER catalytic pathway for Ni in elevated KOH concentrations. The corresponding Nyquist plots of the EIS of Ni and HX are shown in Figure S3 in the SI.

Activation through Potential Cycling

During the CVs for the activity measurement, the potential is swept between 1.2 and 2.0 V vs. RHE. This potential window covers surface reactions of Ni itself. In alkaline media, the metallic Ni^0 surface is oxidised to $Ni(OH)_2$ at about 0.3 V vs. RHE.[55] If no higher potentials are applied, this oxidation is fully reversible.[55,56] However, upon applying higher potentials, this oxidation becomes irreversible.[56] During the first conditioning CV, this oxidation is visible as shown in Figure S4 in the SI. Further conditioning CVs, however, show no Faradaic processes. With a further increase of the potential just before the onset of the OER, the voltammogram reveals a peak at about 1.45 V vs. RHE, which stems from the oxidation of Ni(II) to Ni(III) and, thus, the formation of NiOOH.[57] During the backwards scan, a corresponding reduction peak is observable. However, the charge of the reduction peak is reported to be smaller than that of the oxidation peak, indicating an incomplete reversibility of the NiOOH-formation.[57] As the OER takes place at higher potentials, it appears plausible that the NiOOH formation majorly contributes to the OER activity, which is also confirmed by Lu *et al.*[58] and Magnier *et al.*[36].

Figure 4a illustrates a series of consecutively recorded CVs for Ni in 1 M KOH across the Ni(II)/Ni(III)-redox peaks in the 1.0 to 1.6 V vs. RHE range at 200 mV s^{-1}. The maximum currents of the anodic peak shifts to higher potentials from 1.40 to 1.44 V vs. RHE while the cathodic peak shifts to lower potentials from 1.37 to 1.34 V vs. RHE. Moreover, the maximum currents of both oxidation and reduction peaks increase with increasing number of cycles. Due to the incomplete reversibility of the NiOOH formation, this increase of the maximum currents can be correlated to a growth of the NiOOH-layer.[57]

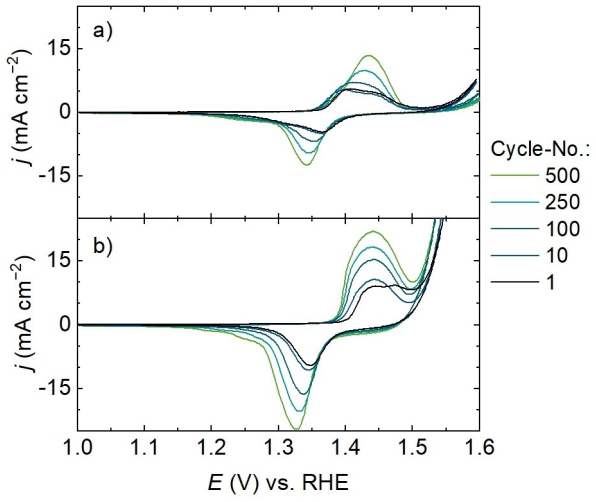

Figure 4. Series of 500 consecutively recorded CVs across the Ni(II)/Ni(III)-redox peaks in the range of 1.0 to 1.6 V vs. RHE at 200 mV s^{-1} for nickel (a) and Hastelloy® X (b) in 1 M KOH electrolyte. Only the 1st, 10th, 100th, 250th and 500th CVs are shown.

Likewise, Fe- and Co-surfaces experience surface oxidation comparable to Ni and, thus, formation of surface hydroxides and oxyhydroxides under anodic polarisation in alkaline media.[59,60] The series of CVs recorded with HX are summarized in Figure 4b, revealing much larger oxidation and reduction peaks in the Ni(II)/Ni(III)-redox potential area. Any contribution from molybdenum oxide-involving redox couples to the Ni(II)/Ni(III)-redox peaks can be excluded due to their appearance at much lower potentials.[51] Similarly, the Fe(II)/Fe(III)-redox couple appears at much lower potentials and, thus, does not contribute to the peak currents.[49,61] However, the presence of Fe(III) species in the proximity of Ni, as in this alloy, is reported to inhibit Ni(II) oxidation, which results in a shift of the peak current to a higher potential at about 1.44 V vs. RHE.[44–46,58] Interestingly, the oxidation peak does not further shift to higher potentials with increasing number of cycles but remains constant. The greater charge of the redox-peaks of the HX alloy might be accounted to an overlay of the Ni(II)/Ni(III)-redox couple with the Cr(III)/Cr(VI)-redox couple which can be expected at slightly lower potentials.[59] Additionally, the small content of Co might also add to the larger charge as the Co(III)/Co(IV)-redox couple can also be expected in proximity to the NI(II)/Ni(III)-redox couple.[62] However, the fast scan rate of 200 mV s^{-1} as well as the contributions of other alloying metals potentially cause merging of multiple redox processes into one observable peak-couple. The 500 consecutively recorded CVs for all investigated substrates are shown in Figure S5 in the SI.

Generally, the growth of the NiOOH-layer as well as other transition metal (oxy−)hydroxide layers and, thus, increase in active species, is expected to facilitate the OER electrocatalysis. Therefore, the consecutive potential cycling across the Ni(II)/Ni(III)-redox couple should exhibit an activating effect on the electrode. Here, no observable differences can be found on scanning electron microscopy (SEM) images exemplary taken for nickel and HX in untreated and activated state (Figure S6 for Ni and S10 for HX in the SI). However, this growth of an oxygen-containing surface layer is detectable by qualitatively recorded energy dispersive X-ray (EDX) mappings showing a detectable amount of surface oxygen species after activation which was not detectable in the untreated state, as shown in the Figures S7 and S8 for Ni and Figure S11 and S12 for HX in the SI.

Figure 5 presents the overpotentials η_{10} for all tested electrode substrates determined at a current density of 10 mA cm^{-2} before and after the consecutive potential cycling across the Ni(II)/Ni(III)-redox peaks. Indeed, an activating effect for all substrates can be observed as the overpotentials after the potential cycling are lower than those prior to this treatment. Interestingly, the relative decrease in overpotential seems

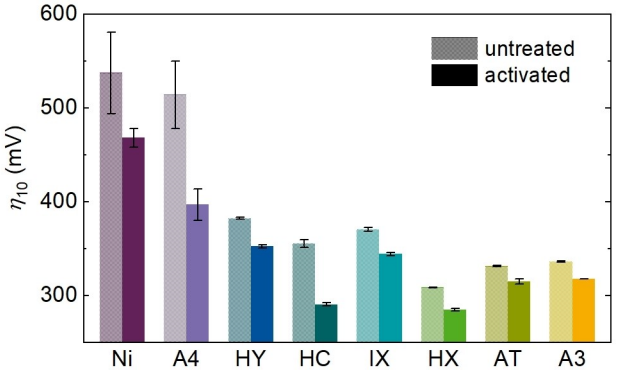

Figure 5. Comparison of overpotentials η_{10} of all tested electrode substrates determined at current density of 10 mA cm^{-2} from forward scans with a scan rate of 10 mV s^{-1} in untreated state and after activation via 500 consecutive potential cycles across the Ni(II)/Ni(III)-redox peaks. Generally, all substrates were measured after recording 30 conditioning CVs with a scan rate of 100 mV s^{-1} in the non-Faradaic potential region of 0.4–1.2 V vs. RHE.

to be higher for initially less active materials such as Ni and A4. Ni shows an overpotential decrease of 12.9% while A4 shows the largest decrease among all tested materials of 22.8%. All other, initially much more active materials show significantly lower relative overpotential reductions with the exception of HC, which exhibits the second largest decrease of 18.2%. With this large decrease, the overpotential of activated HC with 291 ± 2 mV is close to that of activated HX with 285 ± 2 mV as the most active material. H2, IX and HX show a comparably similar relative decrease in overpotential of 7.8, 7.1 and 7.2% respectively. The lowest decreases in overpotential can be found for the iron-base alloys A3 and AT with 5.6 and 5.0%, respectively, which might be explained by the low Ni-contents in these alloys. Here, only a small fraction of the total electrode material can be activated via the growth of the NiOOH-layer. The degree of activation roughly corresponds to the findings of Magnier *et al.*[36] who have described a correlation of the Fe/Ni-ratio in Fe–Ni-alloys on the degree of activation through ageing or potential cycling. While alloys with a low Fe/Ni-ratio in the bulk can incorporate Fe through deposition from impurities in the electrolyte into the growing active NiOOH layer, too high Fe/Ni-ratios lead to the formation of only small active layers,[36] which corresponds well with the low degree of activation found here for AT and A3.

Typically, the electrochemically active surface area (ECSA) of the electrode differs from its physical surface area. Among different methods for the ECSA determination, one utilizes the integration of peak areas of surface oxidation reactions in voltammograms. Generally, the peak area denotes a total transferred charge and, thus, directly corresponds to the number of atoms involved in the electron transfer of the surface oxidation reaction. For Ni-based materials, this proportionality was shown by Grdeń *et al.*[63] for the Ni(0)/Ni(II)-oxidation and for the Ni(II)/Ni(III)-oxidation by Jeon et al.[64] and Anantharaj *et al.*[65]. While the influence of the other alloying elements and the history of the electrodes is unquantified, it could be assumed that the increase of oxidation peak area during the consecutively recorded CVs is proportional to the increase in ECSA of each substrate. Figure S14 and S15 show increasing oxidation peak areas for almost all substrates and the corresponding increase factor is listed in Table S16. While the procedure of consecutive potential cycling lead to an increase in activity for all substrates as shown in Figure 5, the degree of activity gain does not correlate to the increase in oxidation peak area while A3 even shows a slight decrease. Hence, it can be followed that the increase in activity does not solely result from an increase in the ECSA.

Stability Measurements

CP measurements record the behaviour of the electrode potential over time and, thus, allow for stability assessment of the electrodes during OER.[66] As a constant current density of 10 mA cm^{-2} is applied, an increase in potential necessary to maintain the current denotes a decrease in activity. Stability measurements were performed for 24 h on HX, as the most active substrate, and Ni in both untreated state and activated state (via potential cycling), as shown in Figure 6.

Untreated Ni as the least active electrode shows the highest starting potential of about 1.58 V vs. RHE. This is interestingly much lower than the overpotential η_{10} determined at a current density of 10 mA cm^{-1} during CV at 10 mV s^{-1} which underlines the high fluctuations of the OER activity determination of pure Ni as represented by the large error bars in Figures 2b and 5. During the first six hours of CP, the potential of untreated Ni increases to about 1.65 V vs. RHE. In the following, the potential decreases with a lower, almost linear slope to about 1.73 V vs. RHE, resulting in a deactivation of about 150 mV over the course of 24 h. This comparatively strong deactivation might explain the difficulty of the reproducibility and high fluctuations in the activity determination of untreated Ni, as the time spent in contact with the electrolyte, the history of the electrode as well as its precise handling can lead to premature deactivation even before the start of the measurements. As expected, the Ni electrode activated through repeated potential cycling across

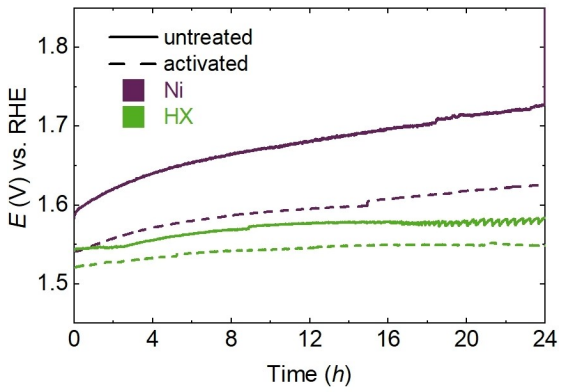

Figure 6. Chronopotentiometric measurements of Ni and Hastelloy® X (HX) in both untreated state and activated state (via 500 consecutive potential cycles across the Ni(II)/Ni(III)-redox couple) in galvanostatic mode at a constant current density of 10 mA cm^{-2}. Potential jumps and oscillations can be attributed to bubble detachment and refilling of the ultra-pure water.

the Ni(II)/Ni(III)-redox couple shows a lower starting potential of about 1.54 V vs. RHE. Here, an increase in the potential to about 1.58 V vs. RHE is observable during the first six hours. Subsequently, the potential increases with a lower slope to about 1.63 V vs. RHE after 24 h, resulting in a deactivation of about 90 mV during 24 h of CP. This generally lower increase in potential compared to the untreated Ni suggests that the NiOOH-layer formed through the activating potential cycling exhibits increased stability in OER electrocatalysis, possibly by protecting the electrode from passivation. Furthermore, in the regard of its OER performance, pure nickel is very sensitive to the presence of iron.[44,45]

Untreated HX exhibits a starting potential of about 1.54 V vs. RHE which matches quite well with the overpotential η_{10} determined at a current density of 10 mA cm^{-1} during CV at 10 mV s^{-1}. A slight increase in potential is visible during the first ten hours and then remains almost constant at about 1.58 V vs. RHE. In addition to the activity enhancing effect, the other alloying metals in HX appear to also stabilise the OER performance of the nickel-base alloy. The oscillation of the potential starting after about 20 h can be accounted to surfacing blockage through bubbles and consecutive detachment. The starting potential of activated HX with 1.52 V vs. RHE is about 21 mV lower than that of untreated HX and is, thus, consistent with the decrease in overpotential η_{10} determined through CV as shown in Figure 5. The activation procedure does not appear to impact the stability of the OER electrocatalysis of HX as the potential difference between untreated and activated HX remains more or less constant. For both untreated and treated HX during chronopotentiometric measurements, the insulating acrylic layer was found to gradually detach from the substrate and, thus, the available active surface area slightly increases. Therefore, the true deactivation of these electrode is expected to be slightly higher than recorded.

SEM images of untreated Ni and HX before and after 24 h of CP can be found in Figures S6 and S10 in the SI, respectively. While no significant differences can be observed here, the qualitatively recorded EDX mappings of these electrodes show differences between Ni and HX to some extent. The EDX mappings of untreated Ni before (Figure S7) and after 24 h of CP (Figure S9) show no significant difference and, thus, the deactivation might result from the incorporation or leaching of foreign species below the EDX detection limit. However, the EDX mappings of untreated HX after 24 h of CP (Figure S13) shows a detectable amount of surface oxygen species which is not present for HX before CP (Figure S11). This formation of an oxidised surface layer might therefore counteract the deactivation process observed for pure Ni.

Conclusions

In this work, Ni and seven commercially available nickel containing alloys were electrochemically tested in the alkaline oxygen evolution reaction with 1 M KOH electrolyte and their elementary composition correlated to the corresponding activity. Here, the Fe-, Cr-, Mo- and Co-containing nickel-base alloy Hastelloy® X (HX) exhibits the lowest overpotential and, thus, highest activity. HX and Ni were both applied as OER anodes in 30 wt. % KOH as industrially commonly applied electrolyte. Due to the higher conductivity of the electrolyte, overall higher currents were reached while Ni also showed different OER behaviour.

500 repeated CVs across the Ni(II)/Ni(III) were recorded for all substrates as an activity enhancing procedure because the incomplete reversibility of the Ni(II)-oxidation results in an accumulation of NiOOH as OER active species. This activity-enhancing procedure also significantly increases the poor stability of untreated Ni. HX retains its high OER activity in both untreated and activated state and, thus, exhibits a high OER stability.

Supporting Information

The authors have cited additional references within the Supporting Information.[67]

Experimental section

Materials and Chemicals

Haynes® 230, Hastelloy® X and Inconel® X750 were obtained from Goodfellow Cambridge Ltd., Alloy 400 and nickel foil (99.5 %) from Alfa Aesar. Hastelloy® C22, AISI 316Ti, AISI 303 were obtained from local suppliers. KOH (Chemsolute, $\geq$85 %) was used as obtained and solutions made with ultrapure water.

Electrode Preparation and Cell Setup

The alloy sheets were cut to electrodes of 5 cm length and 1 cm width, ground with SiC-paper (Buehler, P600) in uniaxial, lengthwise direction, and then cleaned via sonication in DI water (5 min) and absolute ethanol (5 min). In order to isolate an active electrode area of 1 cm^2, the whole electrode with the exception of a 1 cm^2 area at the end of the electrode (one side) and a 4 mm wide strip at the top for contacting (both sides) were insulated with an acrylic spray (Jelt Tropicoat). These electrodes (working electrode, WE) were measured in a three-electrode setup with a glassy carbon (GC) sheet counter electrode (CE) of 1×5 cm size at a distance of 15 mm from the WE and a Hg/HgO (1 M KOH, ALS Co., Ltd. RE-61AP) reference electrode (RE) in between with 1 M KOH as electrolyte. All electrochemical measurements were performed at room temperature and recorded with potentiostats/galvanostats (Metrohm Autolab PGSTAT204 or PGSTAT302 N).

Electrochemical Experiments

The electrochemical experiments of nickel and the different nickel-base and nickel-containing alloys in the OER were performed on a 1 cm^2 polished area of the flat sheet electrodes. Initially, the surfaces of the electrodes were conditioned by 30 consecutive CVs from 0.4 to 1.2 V vs. the reversible hydrogen electrode (RHE) at a scan rate of 100 mV s^{-1}.

The applied or recorded potentials E_{pstat} were iR-corrected and referenced to the RHE by adding the constant potential of the Hg/

HgO (1 M KOH) RE measured as 0.915 V vs. RHE against a hydrogen RE (gaskatel, HydroFlex) according to Equation 3.

$$E_{RHE} = E_{pstat} + 0.915\ V - i \times R_u \quad (3)$$

Here, E_{RHE} is the potential referenced against the RHE, i the recorded current and R_u the uncompensated resistance determined from electrochemical impedance spectroscopy (EIS).

Electrochemical activity. The activity of the electrodes was generally determined from the forward scan of the third out of three consecutive CVs recorded in a potential window of 0.085 to 1.085 V vs. Hg/HgO (1 M KOH) at a scan rate of 10 mV s^{-1}.

EIS measurements. All EIS measurements were performed at 1.6 V vs. RHE with a root mean square (RMS) potential amplitude of 10 mV applied at 10 frequencies per decade between 100 kHz and 0.1 Hz. These measurements were also used to determine the uncompensated resistance R_u.

Potential Cycling. Electrode activation through potential cycling across the Ni(II)/Ni(III)-redox peaks were performed by recording 500 consecutive CVs in the potential window from 0.085 to 0.685 V vs. Hg/HgO (1 M KOH) at a scan rate of 200 mV s^{-1}.

Chronopotentiometry. In galvanostatic mode, the current was initially ramped from 0 to 10 mA cm^{-2} with a ramping rate of 0.2 mA cm^{-2} s^{-1}. For stability measurements, chronopotentiometry was performed for 24 h at a constant current of 10 mA cm^{-2}, with the potential measured against Hg/HgO (1 M KOH). In order to counter the loss of water through electrolysis as well as evaporation and, thus, increase in KOH concentration in the electrolyte, ultrapure water was added multiple times during the 24 h-span to refill to the initial filling volume. The current was then ramped down to 0 A with a rate of 0.2 mA cm^{-2} s^{-1}.

Activity measurement in 30 wt. % KOH. The measurements in 30 wt. % KOH (6.9 M) were performed equally to those in 1 M KOH. A Hg/HgO (6 M KOH, ALS Co., Ltd. RE-61AP) reference electrode was used. The applied potentials were iR-corrected and referenced to the RHE by adding the constant potential of the Hg/HgO (6 M KOH) RE measured as 0.943 V vs. RHE. The electrodes were initially conditioned by 30 CVs in the non-Faradaic potential region between 0.4 and 1.2 V vs. RHE with a scan rate of 100 mV s^{-1}. The activity CVs were obtained from the forward scan of the third out of three consecutive CVs recorded from 0.085 to 1.085 V vs. Hg/HgO (6 M KOH) at a scan rate of 10 mV s^{-1}.

SEM images and EDX mappings. A COXEM EM-30AXN electron microscope was used to record SEM images of the electrodes surfaces with acceleration voltages between 10 and 20 kV in secondary electron (SE) mode. EDX mapping were recorded with this electron microscope using the AZtecONE software.

Acknowledgements

This work was funded by the German Federal Ministry of Education and Research (BMBF) within the project H2 Giga QT1.1 PrometH2eus (FKZ 03HY105 A). This study was conducted in connection to our activities in the project "Digitalization in Catalysis" NFDI4Cat–ID: 441926934 funded by German Research Foundation (DFG). Open Access funding enabled and organized by Projekt DEAL.

Conflict of Interests

The authors declare no conflict of interest.

Data Availability Statement

The data that support the findings of this study are available on Zenodo under doi: 10.5281/zenodo.10669810.

Keywords: electrochemistry · water electrolysis · hydrogen production · oxygen evolution reaction · nickel-base alloys

[1] N. Armaroli, V. Balzani, *ChemSusChem* **2011**, *4(1)*, 21–36.
[2] M. Momirlan, T. N. Veziroglu, *Int. J. Hydrogen Energy* **2005**, *30(7)*, 795–802.
[3] B. Ewan, R. Allen, *Int. J. Hydrogen Energy* **2005**, *30(8)*, 809–819.
[4] G. Marbán, T. Valdés-Solís, *Int. J. Hydrogen Energy* **2007**, *32(12)*, 1625–1637.
[5] T. E. Mallouk, *Nat. Chem.* **2013**, *5(5)*, 362–363.
[6] T. Wang, X. Cao, L. Jiao, *Carb Neutrality* **2022**, *1(1)*.
[7] M. A. Khan, H. Zhao, W. Zou, Z. Chen, W. Cao, J. Fang, J. Xu, L. Zhang, J. Zhang, *Electrochem. Energy Rev.* **2018**, *1(4)*, 483–530.
[8] S. A. Grigoriev, V. N. Fateev, D. G. Bessarabov, P. Millet, *Int. J. Hydrogen Energy* **2020**, *45(49)*, 26036–26058.
[9] M. David, C. Ocampo-Martínez, R. Sánchez-Peña, *J. Energy Storage* **2019**, *23*, 392–403.
[10] J. Brauns, T. Turek, *Processes* **2020**, *8(2)*, 248.
[11] H. Dau, C. Limberg, T. Reier, M. Risch, S. Roggan, P. Strasser, *ChemCatChem* **2010**, *2(7)*, 724–761.
[12] M. Yu, E. Budiyanto, H. Tüysüz, *Angew. Chem. Int. Ed.* **2022**, *61(1)*, e202103824.
[13] R. Eisenberg, H. B. Gray, *Inorg. Chem.* **2008**, *47(6)*, 1697–1699.
[14] S. Trasatti, *Electrochim. Acta* **1984**, *29(11)*, 1503–1512.
[15] S. Trasatti, *J. Electroanal. Chem. Interfacial Electrochem.* **1980**, *111(1)*, 125–131.
[16] Y. Matsumoto, E. Sato, *Mater. Chem. Phys.* **1986**, *14(5)*, 397–426.
[17] Z.-Y. Yu, Y. Duan, X.-Y. Feng, X. Yu, M.-R. Gao, S.-H. Yu, *Adv. Mater.* **2021**, *33(31)*, e2007100.
[18] M.-I. Jamesh, X. Sun, *J. Power Sources* **2018**, *400*, 31–68.
[19] M. E. Lyons, M. P. Brandon, *J. Electroanal. Chem.* **2010**, *641(1–2)*, 119–130.
[20] C. C. L. McCrory, S. Jung, J. C. Peters, T. F. Jaramillo, *J. Am. Chem. Soc.* **2013**, *135(45)*, 16977–16987.
[21] J. S. Kim, B. Kim, H. Kim, K. Kang, *Adv. Energy Mater.* **2018**, *8(11)*, 1702774.
[22] F. Lyu, Q. Wang, S. M. Choi, Y. Yin, *Small* **2019**, *15(1)*, e1804201.
[23] C. Wei, R. R. Rao, J. Peng, B. Huang, I. E. L. Stephens, M. Risch, Z. J. Xu, Y. Shao-Horn, *Adv. Mater.* **2019**, *31(31)*, e1806296.
[24] T. Lazaridis, B. M. Stühmeier, H. A. Gasteiger, H. A. El-Sayed, *Nat. Catal.* **2022**, *5(5)*, 363–373.
[25] H. A. El-Sayed, A. Weiß, L. F. Olbrich, G. P. Putro, H. A. Gasteiger, *J. Electrochem. Soc.* **2019**, *166(8)*, F458–F464.
[26] S. Geiger, O. Kasian, A. M. Mingers, S. S. Nicley, K. Haenen, K. J. J. Mayrhofer, S. Cherevko, *ChemSusChem* **2017**, *10(21)*, 4140–4143.
[27] S. Anantharaj, S. R. Ede, K. Karthick, S. Sam Sankar, K. Sangeetha, P. E. Karthik, S. Kundu, *Energy Environ. Sci.* **2018**, *11(4)*, 744–771.
[28] S. Anantharaj, S. Noda, M. Driess, P. W. Menezes, *ACS Energy Lett.* **2021**, 1607–1611.
[29] M. Vuković, *Corros. Sci.* **1995**, *37(1)*, 111–120.
[30] P. W. T. Lu, S. Srinivasan, *J. Electrochem. Soc.* **1978**, *125(2)*, 265–270.
[31] M. E. Lyons, L. D. Burke, *J. Electroanal. Chem. Interfacial Electrochem.* **1984**, *170(1–2)*, 377–381.
[32] C. Abreu, M. Cristóbal, R. Losada, X. Nóvoa, G. Pena, M. Pérez, *Electrochim. Acta* **2004**, *49(17–18)*, 3049–3056.
[33] C. M. Abreu, M. J. Cristóbal, R. Losada, X. R. Nóvoa, G. Pena, M. C. Pérez, *Electrochim. Acta* **2006**, *51(15)*, 2991–3000.
[34] F. Moureaux, P. Stevens, G. Toussaint, M. Chatenet, *J. Power Sources* **2013**, *229*, 123–132.

[35] F. Moureaux, P. Stevens, G. Toussaint, M. Chatenet, *Appl. Catal. B* **2019**, *258*, 117963.
[36] L. Magnier, G. Cossard, V. Martin, C. Pascal, V. Roche, E. Sibert, I. Shchedrina, R. Bousquet, V. Parry, M. Chatenet, *Nat. Mater.* **2024**, *23*, 252–261..
[37] H. Schäfer, S. M. Beladi-Mousavi, L. Walder, J. Wollschläger, O. Kuschel, S. Ichilmann, S. Sadaf, M. Steinhart, K. Küpper, L. Schneider, *ACS Catal.* **2015**, *5(4)*, 2671–2680.
[38] H. Schäfer, D. M. Chevrier, P. Zhang, J. Stangl, K. Müller-Buschbaum, J. D. Hardege, K. Kuepper, J. Wollschläger, U. Krupp, S. Dühnen, M. Steinhart, L. Walder, S. Sadaf, M. Schmidt, *Adv. Funct. Mater.* **2016**, *26(35)*, 6402–6417.
[39] H. Schäfer, K. Küpper, J. Wollschläger, N. Kashaev, J. Hardege, L. Walder, S. Mohsen Beladi-Mousavi, B. Hartmann-Azanza, M. Steinhart, S. Sadaf, F. Dorn, *ChemSusChem* **2015**, *8(18)*, 3099–3110.
[40] N. Todoroki, A. Shinomiya, T. Wadayama, *Electrocatalysis* **2022**, *13(2)*, 116–125.
[41] N. Todoroki, T. Wadayama, *ACS Appl. Mater. Interfaces* **2019**, *11(47)*, 44161–44169.
[42] D. Y. Chung, P. P. Lopes, P. Farinazzo Bergamo Dias Martins, H. He, T. Kawaguchi, P. Zapol, H. You, D. Tripkovic, D. Strmcnik, Y. Zhu, S. Seifert, S. Lee, V. R. Stamenkovic, N. M. Markovic, *Nat. Energy* **2020**, *5(3)*, 222–230.
[43] D. A. Corrigan, *J. Electrochem. Soc.* **1987**, *134(2)*, 377–384.
[44] L. Trotochaud, S. L. Young, J. K. Ranney, S. W. Boettcher, *J. Am. Chem. Soc.* **2014**, *136(18)*, 6744–6753.
[45] S. Anantharaj, S. Kundu, S. Noda, *Nano Energy* **2021**, *80*, 105514.
[46] R. N. Singh, J. P. Pandey, K. L. Anitha, *Int. J. Hydrogen Energy* **1993**, *18(6)*, 467–473.
[47] M. Gong, H. Dai, *Nano Res.* **2015**, *8(1)*, 23–39.
[48] J. Y. Huot, M. L. Trudeau, R. Schulz, *J. Electrochem. Soc.* **1991**, *138(5)*, 1316–1321.
[49] R. S. Schrebler Guzmán, J. R. Vilche, A. J. Arvía, *Electrochim. Acta* **1979**, *24(4)*, 395–403.
[50] C. Schwanke, H. S. Stein, L. Xi, K. Sliozberg, W. Schuhmann, A. Ludwig, K. M. Lange, *Sci. Rep.* **2017**, *7(1)*, 44192.
[51] B. Wang, S. Dong, *J. Electroanal. Chem.* **1994**, *379(1–2)*, 207–214.
[52] J. Yan, L. Kong, Y. Ji, J. White, Y. Li, J. Zhang, P. An, S. Liu, S.-T. Lee, T. Ma, *Nat. Commun.* **2019**, *10(1)*, 2149.
[53] D. E. Hall, *J. Electrochem. Soc.* **1981**, *128(4)*, 740–746.
[54] M. Alsabet, M. Grdeń, G. Jerkiewicz, *Electrocatalysis* **2015**, *6(1)*, 60–71.
[55] M. K. Bates, Q. Jia, H. Doan, W. Liang, S. Mukerjee, *ACS Catal.* **2016**, *6(1)*, 155–161.
[56] M. Alsabet, M. Grden, G. Jerkiewicz, *Electrocatalysis* **2011**, *2(4)*, 317–330.
[57] M. Alsabet, M. Grden, G. Jerkiewicz, *Electrocatalysis* **2014**, *5(2)*, 136–147.
[58] Z. Lu, W. Xu, W. Zhu, Q. Yang, X. Lei, J. Liu, Y. Li, X. Sun, X. Duan, *Chem. Commun.* **2014**, *50(49)*, 6479–6482.
[59] S. Haupt, H. H. Strehblow, *Langmuir* **1987**, *3(6)*, 873–885.
[60] R. D. Cowling, A. C. Riddiford, *Electrochim. Acta* **1969**, *14(10)*, 981–989.
[61] C. Abreu, M. Cristóbal, X. Nóvoa, G. Pena, M. Pérez, C. Serra, *Electrochim. Acta* **2004**, *49(17–18)*, 3057–3065.
[62] L. D. Burke, M. E. Lyons, O. J. Murphy, *J. Electroanal. Chem. Interfacial Electrochem.* **1982**, *132*, 247–261.
[63] M. Grdeń, M. Alsabet, G. Jerkiewicz, *ACS Appl. Mater. Interfaces* **2012**, *4(6)*, 3012–3021.
[64] S. S. Jeon, P. W. Kang, M. Klingenhof, H. Lee, F. Dionigi, P. Strasser, *ACS Catal.* **2023**, *13(2)*, 1186–1196.
[65] S. Anantharaj, P. E. Karthik, S. Kundu, *Catal. Sci. Technol.* **2017**, *7(4)*, 882–893.
[66] F. Zeng, C. Mebrahtu, L. Liao, A. K. Beine, R. Palkovits, *J. Energy Chem.* **2022**, *69*, 301–329.
[67] A. J. Bard, L. R. Faulkner, *Electrochemical Methods – Fundamentals and Applications*, John Wiley & Sons, **2001**, p. 386.

Manuscript received: September 9, 2023
Revised manuscript received: January 31, 2024
Version of record online: February 23, 2024